The Astrophysical Journal Letters, 951:L33 (8pp), 2023 July 10 https://doi.org/10.3847/2041-8213/acdf5c

Ryugu's Anhydrous Ingredients and Their Spectral Link to Primitive Dust from the Outer Solar System

R. Brunetto[1], C. Lantz[1], Y. Fukuda[2], A. Aléon-Toppani[1], T. Nakamura[2], Z. Dionnet[1], D. Baklouti[1], F. Borondics[3], Z. Djouadi[1], S. Rubino[1], K. Amano[2], M. Matsumoto[2], Y. Fujioka[2], T. Morita[2], M. Kukuiri[2], E. Kagawa[2], M. Matsuoka[4], R. Milliken[5], H. Yurimoto[6], T. Noguchi[7], R. Okazaki[8], H. Yabuta[9], H. Naraoka[8], K. Sakamoto[10], S. Tachibana[10,11], T. Yada[10], M. Nishimura[10], A. Nakato[10], A. Miyazaki[10], K. Yogata[10], M. Abe[10], T. Okada[10], T. Usui[10], M. Yoshikawa[10], T. Saiki[10], S. Tanaka[10], F. Terui[12], S. Nakazawa[10], S. Watanabe[13], and Y. Tsuda[10]
[1] IAS, Université Paris-Saclay, CNRS, France; rosario.brunetto@universite-paris-saclay.fr
[2] Tohoku University, Japan
[3] SMIS-SOLEIL, France
[4] National Institute of Advanced Industrial Science and Technology, Japan
[5] Brown University, USA
[6] Hokkaido University, Japan
[7] Kyoto University, Japan
[8] Kyushu University, Japan
[9] Hiroshima University, Japan
[10] ISAS/JAXA, Japan
[11] The University of Tokyo, Japan
[12] Kanagawa Institute of Technology, Atsugi 243-0292, Japan
[13] Nagoya University, Japan
Received 2023 April 18; revised 2023 June 16; accepted 2023 June 19; published 2023 July 10

Abstract

Ryugu is a second-generation C-type asteroid formed by the reassembly of fragments of a previous larger body in the main asteroid belt. While the majority of Ryugu samples returned by Hayabusa2 are composed of a lithology dominated by aqueously altered minerals, clasts of pristine olivine and pyroxene remain in the least-altered lithologies. These clasts are objects of great interest for revealing the composition of the dust from which the original building blocks of Ryugu's parent asteroid formed. Here we show that some grains rich in olivine, pyroxene, and amorphous silicates discovered in one millimeter-sized stone of Ryugu have infrared spectra similar to the D-type asteroid Hektor (a Jupiter Trojan), to comet Hale–Bopp, and to some anhydrous interplanetary dust particles of probable cometary origin. This result indicates that Ryugu's primary parent body incorporated anhydrous ingredients similar to the building blocks of asteroids (and possibly some comets) formed in the outer solar system, and that Ryugu retained valuable information on the formation and evolution of planetesimals at different epochs of our solar system's history.

Unified Astronomy Thesaurus concepts: Asteroids (72); Dust composition (2271); Meteorites (1038); Laboratory astrophysics (2004); Infrared spectroscopy (2285)

1. Introduction

Asteroids are relics of diverse evolutionary states of our planetary system (DeMeo et al. 2015). The compositional heterogeneity of asteroids is the result of complex pre- and postaccretional processes (Brearley 2006; Alexander et al. 2007; Krot et al. 2015), and is responsible for the spectral diversity observed within asteroid classes (Reddy et al. 2015). The composition of asteroid mineral constituents and their assembly are thus key parameters to understand the physicochemical processes operating in the protoplanetary disk and/or in the asteroidal parent bodies all along the solar system's history (Grady & Wright 2006; Scott 2007).

(162173) Ryugu is a small and dark C-type near-Earth asteroid that originated from either the Polana or Eulalia primitive asteroid families (de León et al. 2018; Tatsumi et al. 2021). It is a porous, hydrated, and carbon-rich asteroid reassembled from fragments of a previous larger body (primary parent body) in the main asteroid belt (Watanabe et al. 2019). Hayabusa2 is a JAXA sample return mission which performed two collections at the surface of Ryugu: a first collection (chamber A) close to the equator of Ryugu, and a second collection at the Small Carry-on Impactor artificial crater (chamber C), to access subsurface material (Tachibana et al. 2022). In 2020 December Hayabusa2 returned to Earth 5.4 g of Ryugu's material. The collected samples have been kept in an N_2 environment at the JAXA Curation Center, where they are nondestructively precharacterized (Yada et al. 2021). Ryugu bulk samples mainly consist of millimeter to submillimeter-sized rugged and smooth particles. A JAXA-led phase of initial analysis started in mid-2021, with six international teams (Nakamura et al. 2023; Okazaki et al. 2022; Yokoyama et al. 2023; Naraoka et al. 2023; Noguchi et al. 2023; Yabuta et al. 2023) providing the first general look at Ryugu.

From the Hayabusa2 orbital data, Ryugu appeared as a very dark object dominated by ubiquitous hydrated silicates, produced by aqueous alteration in Ryugu's parent body (Kitazato et al. 2019). While the near-infrared spectra of Ryugu showed little variations down to meter scales, surface images by the MASCOT lander and infrared (IR) hyperspectral

imaging by the Curation Facility revealed heterogeneities at the submillimeter scale (Jaumann et al. 2019; Pilorget et al. 2021). Spectral absorptions at 2.7 and 3.4 μm implied an indigenous aqueous alteration and a C-rich composition, matching the global average of Ryugu and confirming the representativeness of the samples (Pilorget et al. 2021).

Results from the initial analysis teams indicated that Ryugu has elemental, mineral, organic, and isotopic compositions and a history of aqueous alteration that are clearly similar to those of carbonaceous chondrites of Ivuna-type (CI) meteorites, compared to those of other carbonaceous chondrites (CCs). Many coarse samples of Ryugu are breccias consisting of 10–500 μm sized fragments. The "Stone" initial analysis team showed that it is possible to detect lithologies associated to different fragments in millimeter-sized Ryugu particles called "stones" (Nakamura et al. 2023). Elemental maps show chemical heterogeneities between fragments within the same stone, usually with sharp boundaries. The major lithology consists of aqueously altered minerals: the dominant phase is a phyllosilicate-rich (mainly Mg-rich saponite and serpentine) matrix with abundant iron sulfides (pyrrhotite and pentlandite), carbonates (breunnerite and dolomite), magnetite, and hydroxyapatite. The phyllosilicate-carbonate rich lithology probably formed from an initial olivine-pyroxene-rich lithology via low-temperature fluid-rock reactions. The least-altered fragments found in some specific stones contain clasts of the pristine olivine-pyroxene lithology, and they represent objects of prime interest. Yamaguchi et al. (2023) showed that anhydrous silicate grains are extremely rare in Ryugu stones (<0.5 vol%), but they are indigenous to Ryugu, rather than xenolithic materials incorporated later by more recent impacts.

Here we use IR hyperspectral imaging to analyze two millimeter-sized Ryugu stones extracted from Chamber A (A0026) and Chamber C (C0002), and in particular to investigate the mineral composition of a few clasts found within C0002. We compare the obtained Ryugu IR spectra of both stones and clasts to observations of asteroids, comets, meteorites, and interplanetary dust particles (IDPs), to study the potential links between the original building blocks of Ryugu's parent asteroid and objects that retained dust from the outer solar system. We use IR spectroscopy as a tool to build a bridge between the large-scale remote sensing observations of asteroids and the laboratory analyses at the submicron scale.

2. Materials and Methods

During the initial analysis, several samples were prepared at Tohoku University and analyzed at the Institut d'Astrophysique Spatiale (IAS) and Source Optimisée de Lumiére d'Energie Intermédiaire du LURE (synchrotron SOLEIL; Rubino et al. 2023). Stone A0026 was analyzed first and its average IR spectrum measured at the Spectroscopy and Microscopy in Infrared using Synchrotron (SMIS) beamline of SOLEIL was presented by Nakamura et al. (2023). Stone C0002 was analyzed by electron microscopy (Nakamura et al. 2023) but the IR spectra were not reported. In this study we show new IR hyperspectral reflectance measurements of A0026 (section prepared by a Xe plasma focused ion beam) and C0002 (a polished section called plate-5). The sample preparations of A0026 and C0002 were reported elsewhere (Nakamura et al. 2023). We verified that the sample preparations did not affect the spectroscopic results, by comparing with IR spectra measured of unpolished Ryugu fragments using the same setup (Dionnet et al. 2022a).

Figure 1 shows a backscattered electron (BSE) microscope image of C0002-plate-5. Several fragments were identified in C0002 with a scanning electron microscope and the associated elemental analysis (Nakamura et al. 2023). We focused on some regions of interest (ROIs) that include clasts rich in anhydrous silicates. We performed a point-to-point micro-IR characterization using a Bruker HYPERION 2000 microscope equipped with a VERTEX 70v Fourier Transform Infrared (FT-IR) spectrometer at Tohoku University (globar source, spectral resolution of 4 cm^{-1}, ambient conditions), with spots of ~100–200 μm at different locations reported in red in Figure 1.

Then we measured the whole section of C0002 using small-scale IR hyperspectral imaging. We used three different FT-IR microscopes at SMIS-SOLEIL (Rubino et al. 2023) to cover a large spectral range 1–100 μm: (1) a synchrotron-radiation-fed microscope equipped with a large mid-IR (MIR) range MCT/B-detector, (2) a far-IR (FIR) bolometer-equipped microscope, (3) an imaging microscope equipped with a 128 × 128 pixel focal plane array (FPA) detector. The spectral resolutions were either 2, 4, or 8 cm^{-1}. MIR hyperspectral maps were acquired in order to assess the compositional heterogeneity at the diffraction limit. For (1) and (2), different apertures were used from 5 to 100 μm. For (3), we used two objectives (×25 and ×15) with fields of view of 420 μm and 700 μm, and pixel sizes of 3.3 μm and 5.5 μm, respectively. Several FPA IR tiles were joined into mosaic hyperspectral images to cover a large fraction of the surface of C0002 (4–5 mm, one mosaic is shown in Figure 1). Close-up hyperspectral images of C0002 were obtained for four ROIs (green squares in Figure 1), which included five clasts previously identified (Nakamura et al. 2023). The corresponding IR maps are reported in Figure 2. A hyperspectral map of A0026 using the same conditions as C0002 is shown in Figure 3. The data obtained with the different microscopes were combined using overlapping ranges to produce average MIR-FIR spectra for A0026 and C0002 at the millimeter scale (Figure 4).

Hyperspectral data analysis was performed in Quasar (https://quasar.codes) using the Orange Spectroscopy toolbox (Toplak et al. 2017), in particular the principal component analysis (PCA). Other relevant parameters extracted from the IR spectra were the main peak position of the Si–O stretching band of silicates (we designate the strongest band in each spectrum as the main Reststrahlen band), and the position of the Christiansen feature (a minimum of the reflectance marking the transition between the volume- and surface-scattering regimes).

3. Results

While a large fraction of the matrix of C0002 shows the typical 10 μm feature of phyllosilicates (Figure 1), characteristic of the major lithology of Ryugu stones, very different silicate spectral features are observed at some special locations. These are easily identified as olivine- and pyroxene-rich clasts, thanks to their spectral shape (Figure 1, top right, also confirmed by an IR RGB image and by the PCA in Figure 1, bottom right and Figure 2, respectively) and peak position (Figure 2, right), and confirmed by a comparison with the Mg elemental map (Nakamura et al. 2023) where olivine and/or pyroxene inclusions appear as bright spots.

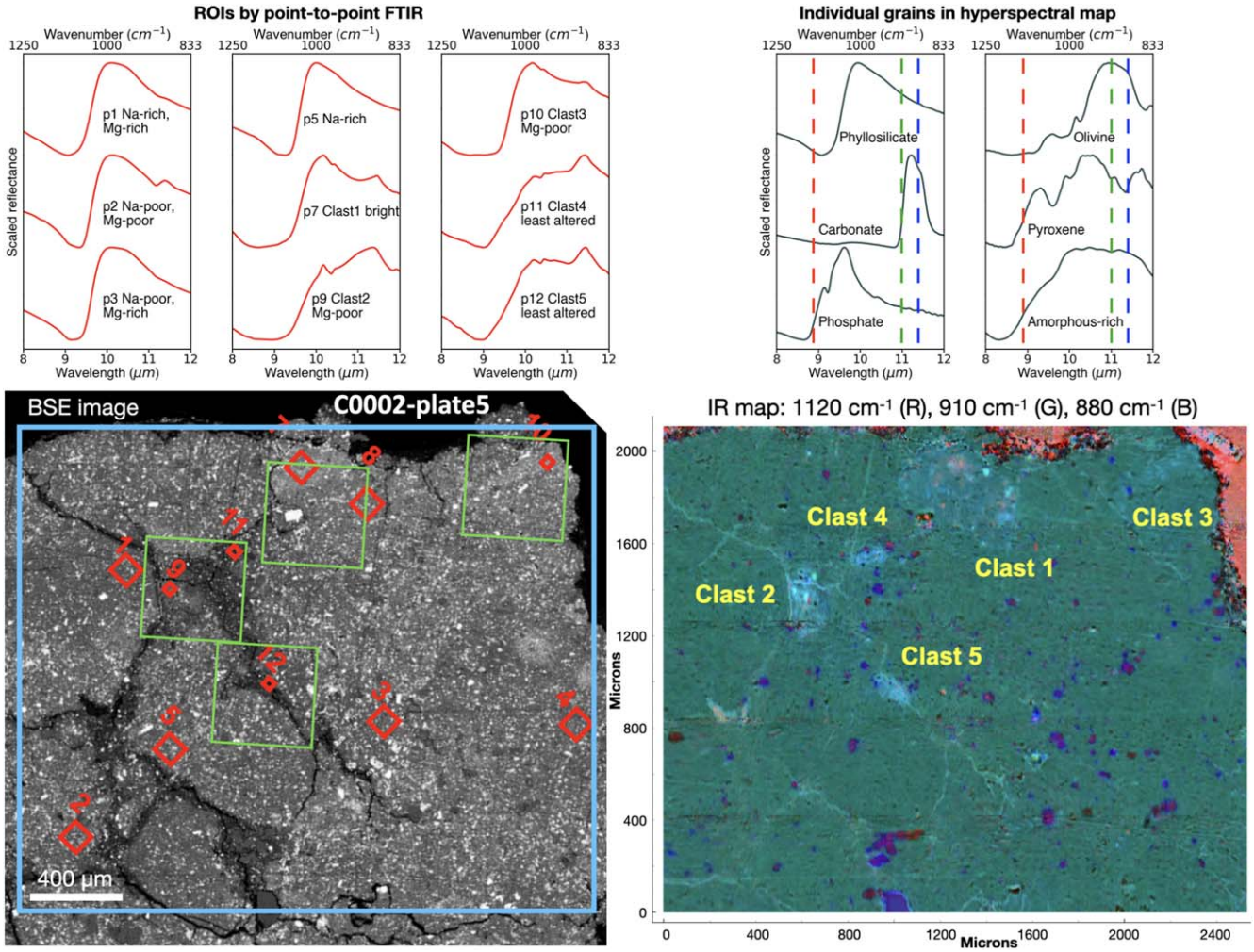

Figure 1. Bottom-left: the location of IR hyperspectral measurements made at SOLEIL (blue rectangle), complemented by point-to-point micro-IR spectra (red squares, the most representative spectra are shown in the top-left panel) acquired at Tohoku University, which are reported on top of a BSE image of C0002-plate-5. Right: the corresponding large IR map of C0002 (pixel size 3.3 μm) showing the reflectance at 1120 cm^{-1} (R), 910 cm^{-1} (G), and 880 cm^{-1} (B), chosen to highlight the differences between typical anhydrous and hydrated phases, as stressed in the top-right panel, which includes examples of spectra of different phases measured in C0002 (grains sizing 10–50 μm). We include a particular grain rich in amorphous phases found in clast 1 (see Figure 2), which also contains minor spectral contributions of olivine at 880 cm^{-1} (11.36 μm) and pyroxene at 960 cm^{-1} (10.42 μm) and 1075 cm^{-1} (9.3 μm). The major lithology (the matrix rich in phyllosilicates is shown in green, plus abundant carbonates in shades varying from dark red to violet and purple, iron sulfides and magnetite in dark brown and dark green, and phosphates in orange) is clearly distinct from the clasts rich in anhydrous phases (pure olivine in teal, olivine-rich in turquoise and cyan, and pyroxene-rich in salmon). Close-up IR images corresponding to the green squares of the bottom-left panel are reported in Figure 2.

The five anhydrous-rich clasts are easily detected, in particular clasts 1 and 5. Anhydrous grains are found in peculiar spots that are clearly visible within the areas where the matrix changes color in the IR RGB images. The majority of these spots are also detected when we trace a map of the peak position of the main Reststrahlen feature (Figure 2). We have arbitrarily selected a few of them and reported the corresponding spectra in the right panel of Figure 2. Most of these inclusions have a double-peak structure, with positions at ~880 cm^{-1} (11.36 μm) and ~980 cm^{-1} (10.20 μm), mainly due to olivine, with minor contributions of pyroxene. The peak positions (Hamilton 2010) of the pure olivine grains (such as G9, G12, and G16) indicate variable ratios of Mg/(Mg +Fe) = 0.20–0.90, depending on the olivine grain size (in agreement with Nakamura et al. 2023) but also on the band used (because of complex scattering effects). Finally, a few inclusions (such as G6 and G8) show Christiansen features at longer wavenumbers due to the spectral contribution of pyroxene at ~1075 cm^{-1} (9.3 μm). A very few grains have a large bandwidth, indicating a significant contribution of amorphous phases. All these features are totally absent from A0026 (Figure 3).

The anhydrous grains in C0002 sum up a very tiny fraction of the section. Based on Figures 1 and 2, we evaluated that the more pristine lithologies constitute less than 6% of C0002, and the anhydrous grains in them constitute less than 5% of their surface, i.e., less than 0.3% with respect to the total surface of C0002, in agreement with independent measurements of another sample (C0009, Yamaguchi et al. 2023).

While the spectra shown in the top right of Figure 1 are measured at the diffraction limit, the contribution of the olivine is also visible at larger scales (~100–200 μm) in the spectra of the ROIs measured in Japan (Figure 1, top left). Olivine bands completely modify the overall IR signature of these ROIs, but their contribution disappears in the average spectrum of C0002 measured over 4–5 mm (Figure 4). This indicates that the detection of lithologies in Ryugu samples with different degrees of alteration (and in particular the more pristine

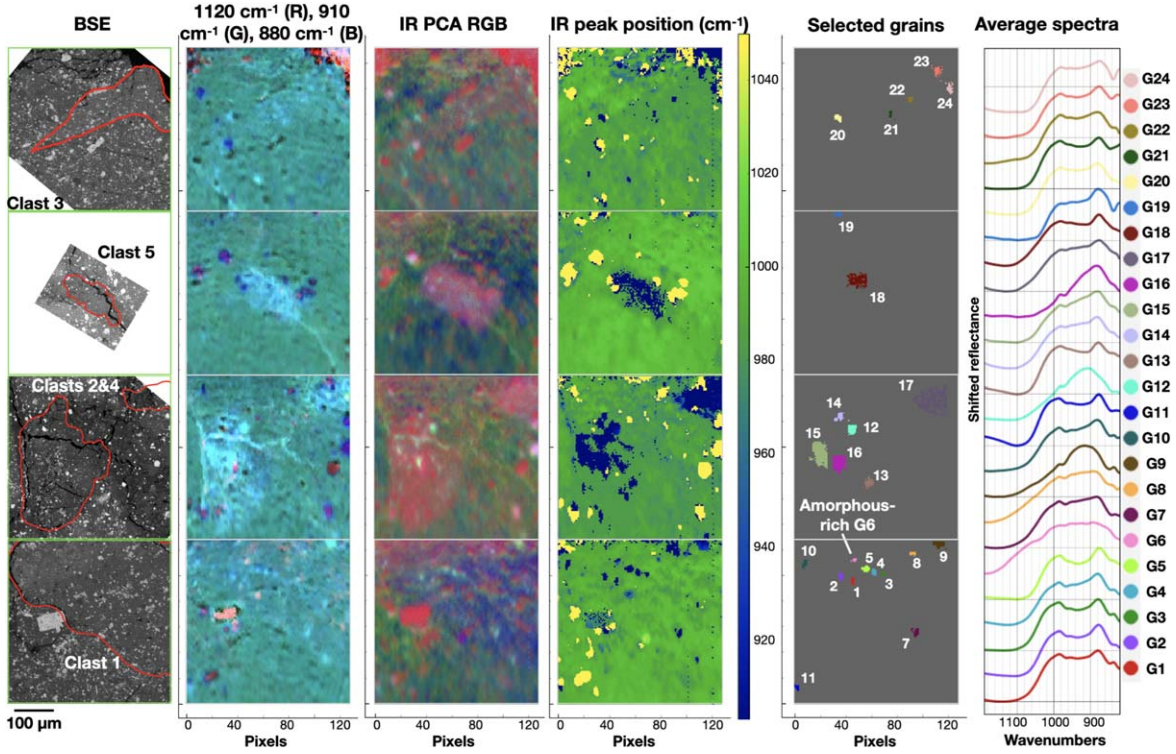

Figure 2. IR maps for four ROIs containing clasts 1–5 in C0002 (see their locations in Figure 1). The four chosen ROIs are piled up for a quick visualization, and also for treating them as a unique and consistent data set. First column (left): zoomed BSE images. Second: the reflectance at 1120 cm^{-1} (R), 910 cm^{-1} (G), and 880 cm^{-1} (B), chosen to highlight the differences between typical anhydrous and hydrated phases (see Figure 1 for a complete map). Third: results of a PCA (R = PC1, G = PC2, and B = PC3) of the spectra around the 10 μm feature. Fourth: map of the peak position of the main Reststrahlen feature (the strongest band in each spectrum). Blue pixels are grains dominated by anhydrous phases, while yellow grains are mainly carbonates. Fifth: a selection of pixels of the anhydrous grains, whose average spectra are reported in the sixth column (right). One of them is highlighted as an amorphous-rich grain. The anhydrous grains represent less than 5% of the chosen ROIs, which means they are even less abundant with respect to the total volume of C0002.

olivine-pyroxene-rich lithology) requires submillimeter spatial resolution and relatively large stones to maximize the chances of discovery. Other lithologies with variable amounts of Na and Mg (Nakamura et al. 2023) show some spectral variations of the 10 μm band, as it can be seen in points 1, 2, 3, and 5 of Figure 1, especially in terms of the relative band ratio between the main Si–O band and its right shoulder, but no clear trend with composition emerges. Overall, these variations remain very small when compared to the clasts containing olivines and pyroxenes (points 7, 9, 10, 11, and 12).

We compared the average spectra of A0026 and C0002, and a few selected ROIs and points of the hyperspectral maps of C0002 (all in reflectance space, with IR absorbance spectra of some IDPs; Brunetto et al. 2011; Merouane et al. 2014; Maupin et al. 2022) and CCs (Lantz et al. 2017; Dionnet et al. 2022b) from different classes (CM, CI, and C2-ung, and also CO, CV, and CK, all in reflectance space), most of them acquired with similar setups. A selection of relevant spectra is reported in Figure 4. We also performed a comparison with some of the available IR remote sensing spectra of asteroids (mostly from ISO and Spitzer; Barucci et al. 2002; Emery et al. 2006; Licandro et al. 2011, 2012; Takahashi et al. 2011; Marchis et al. 2012; Vernazza et al. 2017), plus asteroid Bennu by OSIRIS-REx (Hamilton et al. 2019), and comet Hale–Bopp (Crovisier et al. 1997), all in emissivity space.

The spectra of Figure 4 are characterized by the presence of strong Si–O stretching and bending modes of silicates in the 10 and in the 22 μm regions, whose positions and shapes are sensitive to their compositions and hydration states. The band positions and profiles of the average large-scale spectra of C0002, A0026, Tagish-Lake, Alais, and Orgueil are typically associated with phyllosilicates, while in the case of carbonaceous chondrites of Mighei-type (CMs) they show a mixture of matrix phyllosilicates with anhydrous silicates in chondrules and the matrix. Looking in more detail, C0002 shows a peak position shifted toward longer wavelengths and a stronger shoulder at about 10.7 μm with respect to A0026. Selecting matrix spectra in both stones, we found that these differences are not due to the small anhydrous clasts, but rather to the different compositions of the matrix phyllosilicates. In the spectra of IDP L2021C5 and of clast 2 in C0002, bands associated with olivine and pyroxene show up (Jaeger et al. 1994; Koike et al. 2003), in particular at 880 cm^{-1} (11.36 μm) for olivine, and 960 cm^{-1} (10.42 μm) and 1075 cm^{-1} (9.3 μm) for pyroxene, plus several olivine bands in the FIR at 606 cm^{-1} (16.5 μm), 505 cm^{-1} (19.8 μm), 417 cm^{-1} (24.0 μm), 362 cm^{-1} (27.6 μm), and 296 cm^{-1} (33.8 μm), and potential detections of pyroxene bands at 641 cm^{-1} (15.6 μm), 337 cm^{-1} (29.7 μm), and 266 cm^{-1} (37.6 μm). In the anhydrous objects, the position of the main Christiansen feature shifts toward longer wavenumbers (shorter wavelengths) when the 1075 cm^{-1} (9.3 μm) pyroxene band is present. The different positions of the Christiansen feature between Ryugu stones and CIs are explained by the presence of sulfates in the CIs formed by terrestrial alteration, whose bands overlap with the Christiansen feature of phyllosilicates (Noun et al. 2019).

For most asteroids we only considered the range around the 10 μm band, because the FIR was too noisy to perform a meaningful comparison. Even so, some asteroid spectra are much noisier than the laboratory spectra, so extracting the peak positions and the Christiansen feature as we usually do for

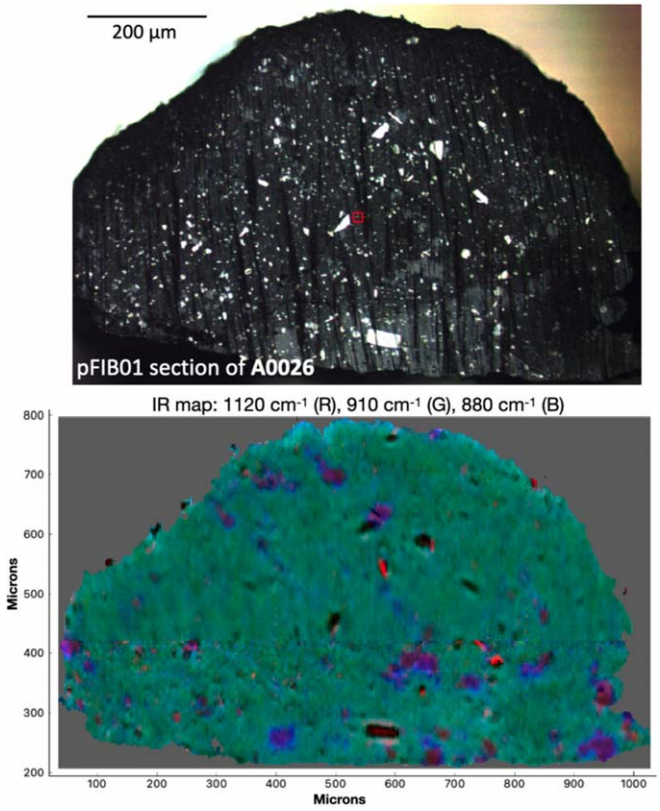

Figure 3. Top: optical image of a pFIB section of A0026. Bottom: IR map (pixel size 3.3 μm, 3 × 2 tiles with an imperfect joining of the upper and lower tiles) using the same color code and the scale of reflectance as C0002 in Figure 1. The major lithology (the matrix rich in phyllosilicates is shown in green, plus abundant carbonates in blue and iron sulfides and magnetite in red and pink, respectively) dominates A0026, but different from C0002 there is no detection of clasts rich in anhydrous phases.

meteorites would be challenging. Instead, we performed a PCA over the considered spectral range. We report the result in Figure 5, where we also added a few meteorites for comparison (Lantz et al. 2017; Hanna et al. 2020; Hewins et al. 2021; Dionnet et al. 2022b). PC2 (positive features at ∼9.3 μm and ∼11.3 μm and a negative feature at ∼9.9 μm) is particularly efficient in separating the hydrated from the anhydrous objects, while PC1 (a positive feature at ∼9.4 μm and a negative feature at ∼11.5 μm) and PC3 (positive features at ∼8.9 μm and ∼10.4 μm and negative features at ∼9.7 μm and ∼11.4 μm) act together to separate olivine from pyroxene in the anhydrous objects, and different degrees of aqueous alteration for the hydrated objects.

An important caveat about this PCA is that asteroids are measured in emissivity space, while meteorites and Ryugu are measured in reflectance space. MIR emissivity spectra of silicates are very sensitive to surface grain size or roughness and the geometry of the observation. The Reststrahlen bands can be detected as maxima or minima, depending on the interplay between volume and surface scattering (Emery et al. 2006). Many factors can alter scattering regimes: hyperfine opaques (Sultana et al. 2023), regolith porosity (Martin et al. 2022), different salts (Izawa et al. 2021), and even environmental conditions (Donaldson Hanna et al. 2017). Here, we assembled the spectra with all the Reststrahlen bands as maxima, for simplicity. A more precise comparison between remote sensing spectra and laboratory spectra should be performed in the context of scattering regimes and it would require estimation of optical constants from the lab data and their insertion into scattering models (Emery et al. 2006). This exceeds the goals of this work and shall be performed in further studies.

4. Discussion

Generally speaking, the IR reflectance spectra of the two Ryugu stones show similarities with the spectra of CIs, in terms of overall spectral shape and peak position of the main Reststrahlen silicate features. Even if similar to CIs, Ryugu spectra have some tiny differences, probably due to a different history of alteration, both on Earth and/or on the original parent bodies. We can see this, for instance, by looking at the peak positions of the Si–O stretching and bending modes (Figure 4), which probably reflect slightly different compositions of the phyllosilicates. According to the PCA, Ryugu stones, CIs, and hydrated IDPs draw a spectral pattern (arrows in Figure 5) which goes, in a scale of increasing alteration, from the least-altered clasts (points 9, 11, and 12) to the hydrated IDPs (L2079D12 and L2079C18), passing through the less-altered clasts of C0002 (points 7 and 10), the major lithology of C0002 (points 1–5 and the average section), A0026, Alais, Tagish-Lake, and Orgueil. The points from the C0002 clasts thus illustrate the IR spectral variations associated with different lithologies (such a variety of composition is absent in A0026). The IR spectra of the Ryugu samples are clearly different from those of the CMs and other ungrouped primitive meteorites. The clasts in C0002 do not overlap with the CMs, probably due to the absence of chondrules in C0002 and to an alteration history of Ryugu different from that of CMs.

In Figure 5, Ryugu is relatively far from Bennu, which is very close to Murchison and Paris. The Ryugu samples and Bennu are also separated from the other asteroids, which are much larger in size (kilometers versus hundreds of kilometers), probably because these large asteroids have a higher contribution of volume scattering by fine grains or they contain some anhydrous components on their surfaces. The surface of the dwarf planet Ceres contains phyllosilicates and carbonates (de Sanctis et al. 2015), but probably also a pyroxene contribution (Vernazza et al. 2017). Asteroids Hygiea and Eugenia are C-types that were reported to be hydrated based on the remote observation of a 0.7 μm band (Fornasier et al. 2014), but a contribution of enstatite and amorphous silicates has also been suggested for Eugenia (Vernazza et al. 2017), as Figure 5 (bottom) seems to confirm. Cybele is an Xc-type (sometimes classified as C/P in different taxonomies) that also seems to show a visible spectral band due to hydration, in contrast to the X-type Sylvia (Fornasier et al. 2014). Athalia Cb-type and Hektor D-type are both associated with anhydrous asteroid types. PC2 draws a pattern from the anhydrous Sylvia and Athalia toward Ceres through the other C-types. The IDPs L2021C5, L2083G23, and L2083E39 (potentially originating from comets or from D-type or P-type primitive asteroids; Brunetto et al. 2011), comet Hale–Bopp, and Trojan Hektor form a last cluster, clearly separated from the others. These objects are all anhydrous.

Vernazza et al. (2017) suggested that small hydrated bodies might represent the interior of a first generation of large primary parent bodies. If that is the case, the link between the small near-Earth hydrated asteroids and the large primitive main-belt asteroids should be looked for in the remaining unaltered dust from the more pristine lithologies. Then let us

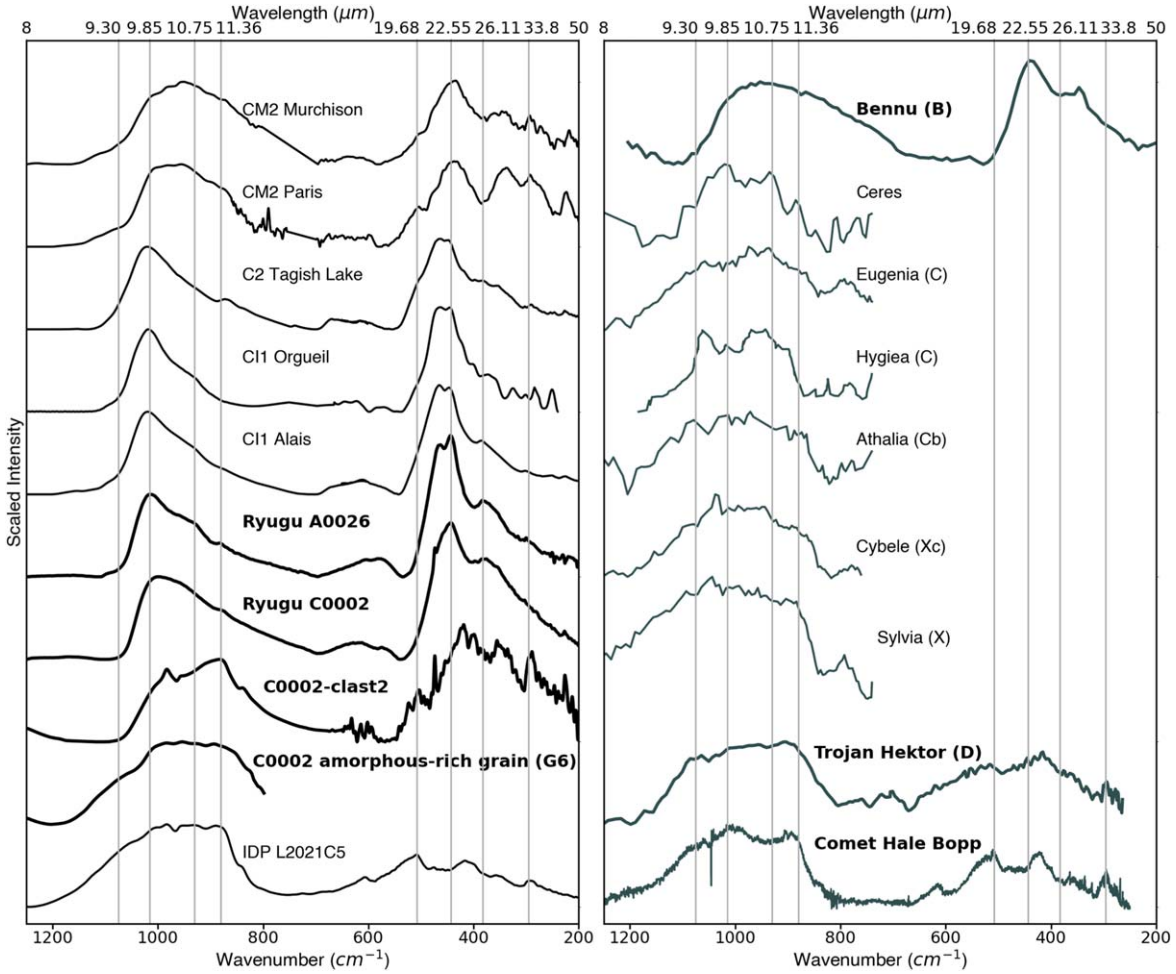

Figure 4. Left: the combined MIR and FIR average spectra of the two Ryugu stones A0026 and C0002 (bold black) are compared in a large spectral range with those measured for different CCs (Lantz et al. 2017; Hewins et al. 2021; Dionnet et al. 2022b) and the anhydrous IDP L2021C5 (Brunetto et al. 2011). The spectra of the olivine-rich clast 2 and of an amorphous-rich grain (see Figure 2) are also included in bold, but the amorphous-rich grain was too small (∼12–15 μm) to measure its FIR spectrum. Ryugu and meteorites are measured in reflectance space, IDPs in absorbance space. Right: remote sensing spectra of different asteroids (we cut the FIR range for objects with spectra too noisy to be compared with lab data), all measured in emissivity space. Asteroids Bennu and Hektor and of comet Hale–Bopp are traced in bold because they have higher signal to noise than the other asteroids. In both panels, vertical gray lines are drawn to guide the eye, as they mark the positions of bands of interest observed in several spectra. All spectra are continuum removed and scaled to unity at the peak of the main Reststrahlen silicate feature around 10 μm. The Reststrahlen bands are shown as maxima, in particular we inverted Bennu's spectrum, showing strong surface scattering (Hamilton et al. 2019), from emissivity space. Other asteroids show the Reststrahlen bands as maxima already in emissivity space, probably because of volume scattering by fine grained silicates (Emery et al. 2006).

focus on a particular grain found within clast 1 (G6, an amorphous-rich grain in Figure 5, size ∼ 12–15 μm), that shows spectral similarity with IDP L2021C5 originated from comets or D-types (Brunetto et al. 2011). G6 is detected both in the elemental map (Nakamura et al. 2023) and in the IR maps of Figures 1 and 2, but unlike the olivine-rich grains its Christiansen feature is blueshifted. Its peculiar spectral shape suggests it is dominated by an amorphous silicate component plus a minor contribution of pyroxene and olivine.

Grains with spectra similar to G6 are found in other clasts of C0002 as well, although very rarely (they are less abundant than pure olivine or pyroxene grains). They can be identified with the anhydrous grains rich in glass with embedded metal and sulfides (GEMS) which were found (Nakamura et al. 2023) in C0002 to be similar in texture and composition (although at least partially altered) to the GEMS found in cometary IDPs, formed by preaccretional processes in the protoplanetary disk (Bradley 1994). The amorphous-rich grains thus represent one of the most interesting reservoirs of anhydrous "cometary-like" dust (a mixture of olivine, pyroxene, and amorphous silicates) found in Ryugu. Their IR spectra prove that there is a link between at least one of the reservoirs from which Ryugu's parent asteroid originated and the reservoir that formed comets and D-type asteroids in the outer protoplanetary disk.

This scenario agrees with independent findings of other analytical techniques within the Initial Analysis Teams. For instance, based on distinct Fe isotopes, Hopp et al. (2022) showed that Ryugu's and CIs' parent bodies possibly formed from a reservoir farther out than other CCs. Also, fluid inclusions of CO_2+H_2O were detected in pyrrhotite, indicating that the parent asteroid of Ryugu formed beyond the H_2O and CO_2 snow lines in the solar nebula (Nakamura et al. 2023), possibly beyond Saturn, where D-type asteroids and some comets also formed. In that region of the disk, based on Ryugu's mineralogy, limited amounts of high-T chondrules and refractory inclusions were present, although the few ones found in Ryugu are probably among the oldest solar system materials (Nakashima et al. 2023). Even more, the relative abundance of the oxygen isotopes of Ryugu's anhydrous primary minerals is similar to that of comet 81P/Wild2, once again suggesting that

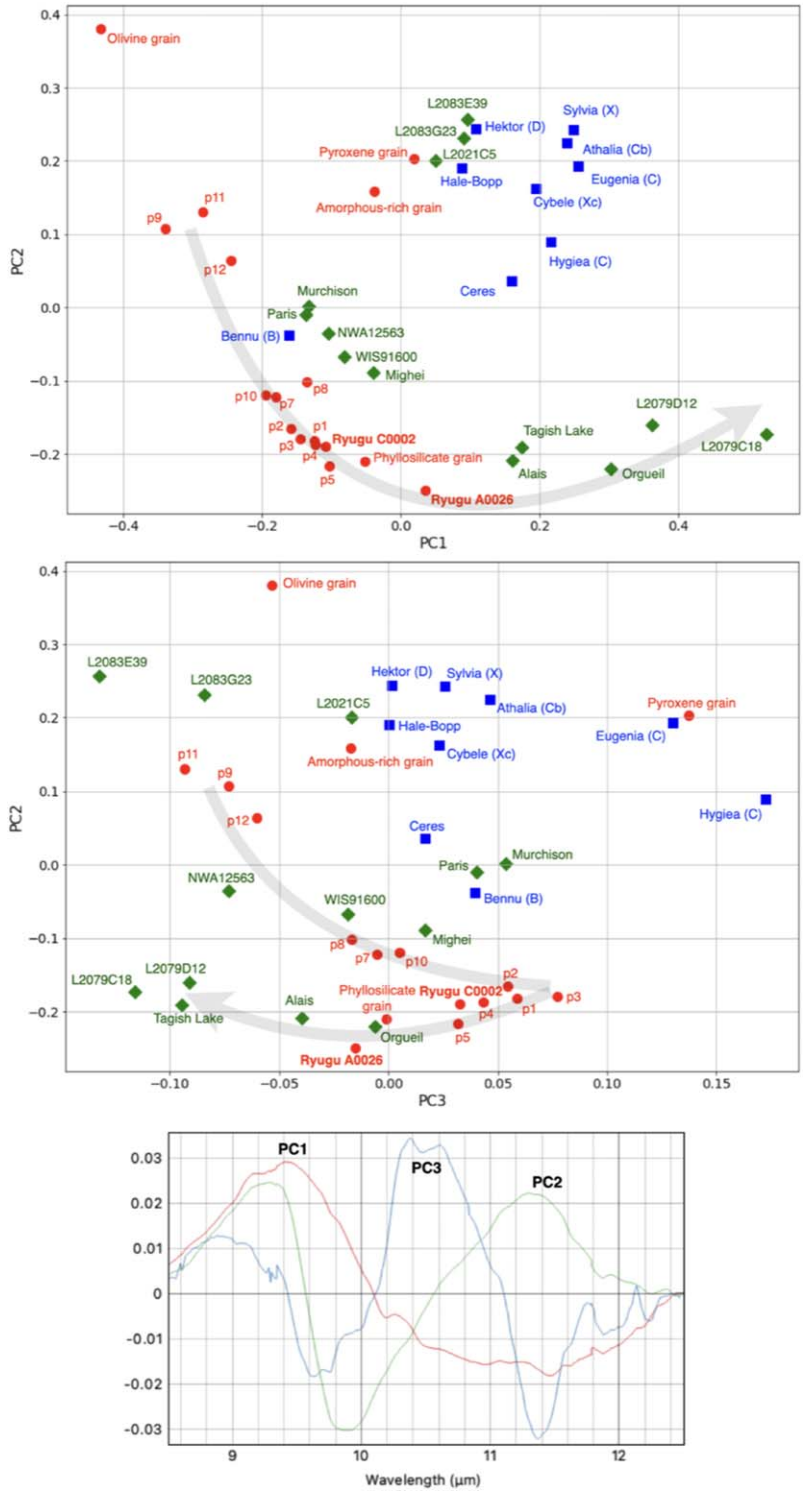

Figure 5. PC2 as a function of PC1 (top) and PC3 (center) for a selection of asteroids (blue squares, emissivity space), meteorites (green diamonds, reflectance space), IDPs (green diamonds, absorbance space), the two Ryugu samples A0026 and C0002, and a few ROIs of C0002 (red dots, reflectance space, showing four ROIs in the main lithology and five ROIs with anhydrous clasts, see Figure 1). The phyllosilicate, olivine, pyroxene, and amorphous-rich grains, shown in Figure 1, are also included. IDPs L2021C5, L2083G23, and L2083E39 are anhydrous (Brunetto et al. 2011; Merouane et al. 2014), while L2079D12 and L2079C18 are hydrated (Maupin et al. 2022). Arrows guide the eye along the alteration pattern. The PCA is performed on the spectra of Figure 4 plus a few additional meteorites and IDPs reported in our previous studies, but only considering the 8.5–12 μm range because it has the highest signal to noise and the most diagnostic features. We assembled the data set in order to have all the Reststrahlen bands as maxima. The components are given in the bottom panel. Remote sensing spectra are measured in emission, while lab spectra are measured in reflection for Ryugu and meteorites, and in transmission for IDPs. However, this should have a minor effect on the PCA, as indicated by the fact that anhydrous IDPs plot very close to Hale–Bopp and Hektor, and that Bennu is very close to Murchison and other CCs. It should also be noted that asteroid spectra can be modified by space weathering, as suggested by laboratory experiments (Lantz et al. 2017; Brunetto et al. 2020).

Ryugu's parent body formed in the outer solar system close to the accretion region of comets (Kawasaki et al. 2022). Finally, both dynamical (Walsh et al. 2011) and spectroscopic (de Sanctis et al. 2015; Takir et al. 2023) studies indicate that a fraction of asteroids that formed beyond Saturn can have been transferred to the inner solar system. All these results, together with the spectral correspondence shown in this work, point at the fact that hydrated C-type asteroids accreted a significant fraction of materials from the same reservoir that produced D-type asteroids and some comets, and subsequent aqueous alteration and dynamical evolution determined the spectral diversity of "primitive" asteroid classes we observe today.

5. Conclusions

Ryugu-returned samples are one of the keys to access the source of asteroid spectral diversity, because their more pristine lithologies contain anhydrous grains which are spectrally similar to some outer solar system primitive bodies. This suggests that Ryugu contains potentially several reservoirs of anhydrous primitive dust, which carry valuable information on the formation and evolution of planetesimals in the proto-planetary disk.

Acknowledgments

This work is part of the multianalytical sequence of the Hayabusa2 "Stone" MIN-PET group, led by T. Nakamura. This work was supported by the Centre National d'Etudes Spatiales (CNES-France, Hayabusa2 mission). Z.D. was supported by a CNES postdoctoral allocation. The microspectroscopy measurements were supported by grants from Region Ile-de-France (DIM-ACAV) and SOLEIL. Special thanks to Y. Kodama, T. Okawa, N. Suzuki, Y. Deguchi, and T. Nishida at TOYO Corporation for their assistance with Xe FIB sample processing. S.T., M.M., H.Y., T.N., R.O., H.Y., and H.N. were supported by the Japanese Society for Promotion of Science (JSPS) grant No. 20H05846. We thank two anonymous reviewers for their useful comments.

Facility: SOLEIL (SMIS).

Software: Quasar (Toplak et al. 2017).

ORCID iDs

R. Brunetto https://orcid.org/0000-0003-3001-9362
C. Lantz https://orcid.org/0000-0003-0974-4770
Z. Dionnet https://orcid.org/0000-0002-3679-6333
D. Baklouti https://orcid.org/0000-0002-2754-7829
F. Borondics https://orcid.org/0000-0001-9975-4301
Z. Djouadi https://orcid.org/0000-0001-5856-494X
K. Amano https://orcid.org/0000-0003-4466-4426
H. Yurimoto https://orcid.org/0000-0003-0702-0533
T. Noguchi https://orcid.org/0000-0001-7211-2595
R. Okazaki https://orcid.org/0000-0003-0177-7527
H. Naraoka https://orcid.org/0000-0002-2373-8759
K. Sakamoto https://orcid.org/0000-0001-5138-5324
S. Tachibana https://orcid.org/0000-0002-4603-9440
T. Yada https://orcid.org/0000-0002-7971-510X
A. Miyazaki https://orcid.org/0000-0001-7427-2285
K. Yogata https://orcid.org/0000-0002-3717-9185
M. Abe https://orcid.org/0000-0003-4780-800X
T. Okada https://orcid.org/0000-0001-6381-8107
M. Yoshikawa https://orcid.org/0000-0002-3118-7475
S. Tanaka https://orcid.org/0000-0002-4874-0417
S. Nakazawa https://orcid.org/0000-0003-4250-1826
S. Watanabe https://orcid.org/0000-0002-5820-2102

References

Alexander, C. M. O. D., Fogel, M., Yabuta, H., & Cody, G. D. 2007, GeCoA, 71, 4380
Barucci, M. A., Dotto, E., Brucato, J. R., et al. 2002, Icar, 156, 202
Bradley, J. P. 1994, GeCoA, 58, 2123
Brearley, A. J. 2006, in Meteorites and the Early Solar System II, ed. D. S. Lauretta & H. Y. McSween (Tucson, AZ: Univ. Arizona Press), 584
Brunetto, R., Borg, J., Dartois, E., et al. 2011, Icar, 212, 896
Brunetto, R., Lantz, C., Nakamura, T., et al. 2020, Icar, 345, 113722
Crovisier, J., Leech, K., Bockelee-Morvan, D., et al. 1997, Sci, 275, 1904
de León, J., Campins, H., Morate, D., et al. 2018, Icar, 313, 25
de Sanctis, M. C., Ammannito, E., Raponi, A., et al. 2015, Natur, 528, 241
DeMeo, F. E., Alexander, C. M. O., Walsh, K. J., Chapman, C. R., & Binzel, R. P. 2015, Asteroids IV (Tucson, AZ: Univ. Arizona Press), 13
Dionnet, Z., Aléon-Toppani, A., Brunetto, R., et al. 2022a, LPICo, 2695, 6078
Dionnet, Z., Aléon-Toppani, A., Brunetto, R., et al. 2022b, M&PS, 57, 965
Donaldson Hanna, K. L., Greenhagen, B. T., Patterson, W. R., et al. 2017, Icar, 283, 326
Emery, J. P., Cruikshank, D. P., & Van Cleve, J. 2006, Icar, 182, 496
Fornasier, S., Lantz, C., Barucci, M. A., & Lazzarin, M. 2014, Icar, 233, 163
Grady, M. M., & Wright, I. 2006, in Meteorites and the Early Solar System II, ed. D. S. Lauretta & H. Y. McSween (Tucson, AZ: Univ. Arizona Press), 3
Hamilton, V. E. 2010, ChEG, 70, 7
Hamilton, V. E., Simon, A. A., Christensen, P. R., et al. 2019, NatAs, 3, 332
Hanna, R. D., Hamilton, V. E., Haberle, C. W., et al. 2020, Icar, 346, 113760
Hewins, R. H., Zanetta, P. M., Zanda, B., et al. 2021, GeCoA, 311, 238
Hopp, T., Dauphas, N., Abe, Y., et al. 2022, SciA, 8, eadd8141
Izawa, M. R. M., King, P. L., Vernazza, P., Berger, J. A., & McCutcheon, W. A. 2021, Icar, 359, 114328
Jaeger, C., Mutschke, H., Begemann, B., Dorschner, J., & Henning, T. 1994, A&A, 292, 641
Jaumann, R., Schmitz, N., Ho, T. M., et al. 2019, Sci, 365, 817
Kawasaki, N., Nagashima, K., Sakamoto, N., et al. 2022, SciA, 8, eade2067
Kitazato, K., Milliken, R. E., Iwata, T., et al. 2019, Sci, 364, 272
Koike, C., Chihara, H., Tsuchiyama, A., et al. 2003, A&A, 399, 1101
Krot, A. N., Nagashima, K., Alexander, C. M. O., et al. 2015, Asteroids IV (Tucson, AZ: Univ. Arizona Press), 635
Lantz, C., Brunetto, R., Barucci, M. A., et al. 2017, Icar, 285, 43
Licandro, J., Campins, H., Kelley, M., et al. 2011, A&A, 525, A34
Licandro, J., Hargrove, K., Kelley, M., et al. 2012, A&A, 537, A73
Marchis, F., Enriquez, J. E., Emery, J. P., et al. 2012, Icar, 221, 1130
Martin, A. C., Emery, J. P., & Loeffler, M. J. 2022, Icar, 378, 114921
Maupin, R., Djouadi, Z., Brunetto, R., et al. 2022, PSJ, 3, 10
Merouane, S., Djouadi, Z., & Le Sergeant d'Hendecourt, L. 2014, ApJ, 780, 174
Nakamura, T., Matsumoto, M., Amano, K., et al. 2023, Sci, 379, 8671
Nakashima, D., Nakamura, T., Zhang, M., et al. 2023, NatCo, 14, 532
Naraoka, H., Takano, Y., Dworkin, J. P., et al. 2023, Sci, 379, abn9033
Noguchi, T., Matsumoto, T., Miyake, A., et al. 2023, NatAs, 7, 170
Noun, M., Baklouti, D., Brunetto, R., et al. 2019, Life, 9, 44
Okazaki, R., Miura, Y. N., Takano, Y., et al. 2022, SciA, 8, eabo7239
Pilorget, C., Okada, T., Hamm, V., et al. 2021, NatAs, 6, 221
Reddy, V., Dunn, T. L., Thomas, C. A., Moskovitz, N. A., & Burbine, T. H. 2015, Asteroids IV (Tucson, AZ: Univ. Arizona Press), 43
Rubino, S., Dionnet, Z., Aléon-Toppani, A., et al. 2023, EP&S, 75, 4
Scott, E. R. D. 2007, AREPS, 35, 577
Sultana, R., Poch, O., Beck, P., et al. 2023, Icar, 395, 115492
Tachibana, S., Sawada, H., Okazaki, R., et al. 2022, Sci, 375, 1011
Takahashi, J., Itoh, Y., & Takahashi, S. 2011, PASJ, 63, 499
Takir, D., Neumann, W., Raymond, S. N., Emery, J. P., & Trieloff, M. 2023, NatAs, 7, 524
Tatsumi, E., Sakatani, N., Riu, L., et al. 2021, NatCo, 12, 5837
Toplak, M., Birarda, G., Read, S., et al. 2017, SRNew, 30, 40
Vernazza, P., Castillo-Rogez, J., Beck, P., et al. 2017, AJ, 153, 72
Walsh, K. J., Morbidelli, A., Raymond, S. N., O'Brien, D. P., & Mandell, A. M. 2011, Natur, 475, 206
Watanabe, S., Hirabayashi, M., Hirata, N., et al. 2019, Sci, 364, 268
Yabuta, H., Cody, G. D., Engrand, C., et al. 2023, Sci, 379, abn9057
Yada, T., Abe, M., Okada, T., et al. 2021, NatAs, 6, 214
Yamaguchi, A., Tomioka, N., Ito, M., et al. 2023, NatAs, 7, 398
Yokoyama, T., Nagashima, K., Nakai, I., et al. 2023, Sci, 379, abn7850